Edge-Localized-Mode Suppression through Density-Profile Modification with Lithium-Wall Coatings in the National Spherical Torus Experiment

R. Maingi,[1] T. H. Osborne,[2] B. P. LeBlanc,[3] R. E. Bell,[3] J. Manickam,[3] P. B. Snyder,[2] J. E. Menard,[3] D. K. Mansfield,[3] H. W. Kugel,[3] R. Kaita,[3] S. P. Gerhardt,[3] S. A. Sabbagh,[4] F. A. Kelly,[3] and the NSTX research team

[1]*Oak Ridge National Laboratory, Oak Ridge, Tennessee 37831, USA*
[2]*General Atomics, San Diego, California, USA*
[3]*Princeton Plasma Physics Laboratory, P.O. Box 451, Princeton, New Jersey 08543, USA*
[4]*Columbia University, New York, New York, USA*

(Received 19 December 2008; published 10 August 2009)

Reduction or elimination of edge localized modes (ELMs) while maintaining high confinement is essential for future fusion devices, e.g., the ITER. An ELM-free regime was recently obtained in the National Spherical Torus Experiment, following lithium (Li) evaporation onto the plasma-facing components. Edge stability calculations indicate that the pre-Li discharges were unstable to low-n peeling or ballooning modes, while broader pressure profiles stabilized the post-Li discharges. Normalized energy confinement increased by 50% post Li, with no sign of ELMs up to the global stability limit.

DOI: 10.1103/PhysRevLett.103.075001 PACS numbers: 52.55.Fa, 52.40.Hf

Periodic ejections of particles and power from the edge of fusion research devices have been observed since the discovery of the high confinement or H mode [1]. These instabilities are termed edge localized modes (ELMs), and they have been observed in nearly all toroidal confinement devices operating in the H mode with sufficient heating power to reach the instability threshold [2,3]. The onset of large (''type 1'') ELMs has been correlated with measured plasma profiles exceeding an operational window on the edge plasma pressure gradient and edge current, imposed by the ideal magnetohydrodynamic (MHD) stability of coupled peeling and ballooning modes [4,5]. Calculations of these ideal MHD limits for future devices, such as the International Thermonuclear Experimental Reactor (ITER), indicate that ELMs are to be expected there also. While ELMs purge the edge plasma of impurities and enable a quasisteady operation in present day devices, they also deliver a pulsed power load that would limit the lifetime of plasma-facing components (PFCs) unless the energy release of each individual ELM was made sufficiently small. Thus, control of ELM size and elimination of ELMs altogether have received high priority in international fusion research. While the quiescent H mode [6] and use of external resonant magnetic perturbations [7] are attractive regimes with suppressed ELMs, the former scenario is thought to require substantial velocity shear, and the latter is thought to require internal coils close to the plasma, both of which present challenges in future devices.

As in other fusion research devices, ELMs are routinely observed [8] in nearly all H-mode discharges in the National Spherical Torus Experiment (NSTX) [9]. H-mode access is facilitated in spherical tokamaks (STs) with fueling from the high-field side [10,11]; however, the difficulty in installing a fully controllable valve in the center stack coupled with the good particle confinement in STs leads to a secular density rise even in most ELMy H-mode scenarios in both the NSTX [12] and the Mega-Amp Spherical Tokamak [13]. Density control in Doublet-3 diverted tokamak (DIII-D) H-mode discharges has been demonstrated with strong in-vessel pumping [14]; in this case, optimal pumping is obtained for particular shapes in which the outer divertor strike point is placed near the pump plenum opening. An alternative being tested in the NSTX is lithium evaporation onto large portions of the divertor PFCs, which in principle could provide density control for a wider variety of boundary shapes while enhancing the energy confinement [15]. In recent experiments in the NSTX, sufficiently thick lithium coatings also resulted in complete ELM suppression [16–19]. The goal of this Letter is to present evidence that the density/pressure profile changes correlated with lithium-wall coatings are responsible for the ELM suppression.

In the remainder of this Letter, we (1) document the change in discharge characteristics and kinetic profiles in pre- and post-lithium discharges, (2) show that the ELM suppression corresponds to stabilization of low-n peeling or ballooning modes based on stability calculations using equilibria constructed from those kinetic profiles, and (3) identify low-n magnetic fluctuation ELM precursors in the range predicted for the pre-lithium stability calculations, where n is toroidal mode number. The final post-lithium, enhanced confinement discharges avoid the edge stability limit but reach the global stability limit with a fraction of the input power of the pre-lithium discharges. We note that while these post-lithium ELM-free discharges can suffer from impurity accumulation and secular radiation increase [20], 3-d magnetic perturbations have been shown to reproducibly trigger ELMs, maintain good confinement, and prevent the impurity buildup [21].

Lithium was introduced into the NSTX vacuum vessel between plasma discharges using a pair of overhead evaporators [18,19]. With a high lithium evaporation

rate (>15 mg/min) and/or coating thickness (>1 g) [17], the energy confinement increased such that the heating power needed to be reduced to avoid the global stability limit. The effect of thick lithium-wall coatings on discharge characteristics is shown for three discharges (black: pre-lithium; red: post-lithium, low power; blue: post-lithium, intermediate power) in Fig. 1. Figure 1(b) shows a step in neutral beam injected power from 2 to 3 MW at 0.45 sec in the post-lithium discharges; the post-lithium discharge with 4 MW of neutral beam injected power (NBI) disrupted shortly after I_p flattop (not shown). The post-lithium discharges showed reduced early density and dN/dt, although the eventual density in the lowest power discharge reached the same value as the reference discharge, partly because of the lack of ELMs [Fig. 1(c)]. Figure 1(d) shows that the stored energy for the 2-MW post-lithium discharge was comparable to the 4-MW pre-lithium discharge and that the energy confinement time normalized by the ITER-97 L-mode global scaling [22] was 50% higher in the post-lithium discharges [Fig. 1(e)]. Following the 2–3 MW step at 0.45 sec, a global MHD instability terminated the high performance phase [blue curve in Fig. 1(d)]. The radiated power was comparable out to 0.48 sec in these discharges, despite higher input in the pre-lithium discharge; i.e., the radiated power fraction increased during the ELM-free H-mode phase [Fig. 1(f)]. Finally, the divertor D_α emission was substantially lower in the post-lithium discharges, indicating reduced recycling, and all signatures of ELM activity vanished [Fig. 1(g)].

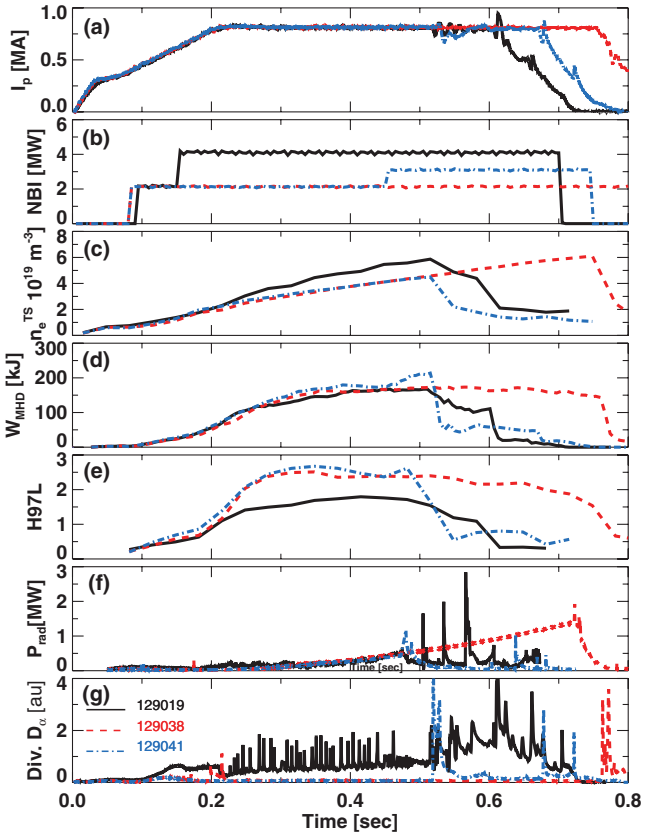

FIG. 1 (color). Comparison of pre-lithium ELMy discharge (black line) and two post-lithium discharges with different NBI power (blue and red lines): (a) plasma current I_p, (b) neutral beam injected power P_{NBI}, (c) line-average density from Thomson scattering n_e^{TS}, (d) stored energy from equilibrium reconstruction W_{MHD}, (e) confinement time relative to ITER-97L scaling, (f) total radiated power P_{rad}, and (g) divertor D_α emission.

The dramatic effect of lithium conditioning on the plasma kinetic profiles for the 2 (post-lithium) and 4 MW (pre-lithium) discharges from Fig. 1 is displayed in Fig. 2. The time slice at $t = 0.415$ sec is displayed because the plasma-outer wall gap was nearly identical, and electron density and temperature (n_e and T_e, respectively) data from the Thomson scattering diagnostic and ion temperature (T_i) data from the charge-exchange recombination spectroscopy (ChERS) diagnostic were centered about the same time window to within 1 msec. In the pre-lithium discharge, the T_e gradient increased outside of $R = 1.42$ m, indicating that $R = 1.42$ m was the top of the H-mode pedestal [Fig. 2(a)]. While the T_e gradient outside of $R = 1.42$ m was unaffected in the post-lithium discharge, the region of reduced gradient from $R = 1.36$–1.42 m was eliminated, effectively shifting the entire profile upward. In contrast, the entire post-lithium n_e profile appears to be shifted inward by about 2 cm, despite having the same plasma-wall gap [Fig. 2(b)]. The density inside of $R = 1.35$ m was also reduced. This profile change is probably due to a reduction in core fueling from the lithium-wall coatings, which is most likely a direct consequence of the 80%–90% reduction in divertor recycling shown in Fig. 1(g). The edge and core post-lithium T_i values were increased [Fig. 2(c)].

To assess the effect of these profile changes on edge stability, an analysis procedure developed in DIII-D was performed [23,24]. The procedure is summarized here: (1) Generate magnetics-only equilibria at the time slices of the Thomson scattering laser pulses using the EFITD

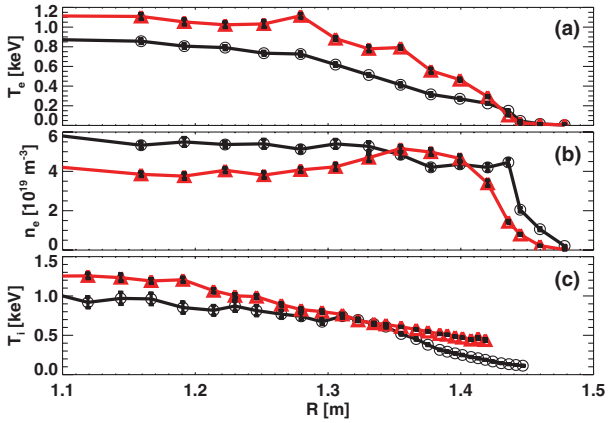

FIG. 2 (color). Profiles for T_e, n_e, and T_i for pre- and post-lithium discharges (black and red lines, respectively).

code [25]. (2) Map the individual n_e, T_e, and T_i profiles to normalized poloidal magnetic flux ψ_N to construct a single profile from the multiple time slice data. For the pre-lithium ELMy discharge, profile data from the last 20% of the ELM cycle are binned [23], with a maximum time window of 100 msec to minimize the effect of the density ramp in Fig. 1. For the post-lithium discharge, multiple profiles using data from 100–200 msec time windows are generated to determine the dependence of the edge stability on density or collisionality. (3) Perform a free boundary kinetic equilibrium fit, using the profiles from step 2 as the target pressure profiles. The target edge current is computed from the neoclassical bootstrap current [26] with Z_{eff} computed from the carbon content as computed from the ChERS data. The stability of these individual equilibria is evaluated with the PEST ideal MHD code [27]. (4) Perform a set of fixed boundary kinetic equilibrium fits (EFITs), while varying the edge pressure gradient at fixed edge current and vice versa. The stability of these various equilibria is evaluated with the ELITE ideal MHD code [4,5] to assess the proximity to the peeling mode (high edge current) and ballooning mode (high pressure gradient) boundaries.

A comparison of the plasma total pressure profile and its radial gradient from representative free boundary kinetic equilibria for the pre- and post-lithium discharges is shown in Fig. 3. Note that a different pre-lithium discharge (no. 129015, programmed identically to no. 129019) was chosen for this analysis, because three Thomson profiles were obtained in a 100 msec window in the last 20% of the inter-ELM period. The pre-lithium discharge had a steep pressure gradient very near the separatrix ($\psi_N = 1$), whereas the peak gradient was shifted inward substantially for the post-lithium discharge [Figs. 3(a) and 3(b)], owing primarily to the change in the n_e profile. In addition, the spatial width of the steep gradient region is larger in the post-lithium discharge (i.e., from $0.8 < \psi_N < 1$), which also enhanced the edge stability.

PEST calculations of the pre-lithium discharge equilibria indicate instability to low-n ($n = 2, 3, 4$) peeling or ballooning modes, with the growth rate peaking for $n = 3$. The maximum linear growth rate was computed at 1.5% of the Alfvén frequency. Figure 3(c) shows that the radial displacement ξ^2 peaks at the low field side plasma edge. In comparison, the post-lithium profiles are stable to these modes.

The fixed boundary kinetic EFITs from step 4 above were shown to be close to the peeling mode instability threshold from ELITE calculations. Figure 3(d) shows an edge stability space diagram of normalized edge current as a function of the normalized pressure gradient [28]. The colors represent contours of the ratio of the mode linear growth rate γ to the diamagnetic drift frequency ω_*. Here the white rectangle and error bars, representing the experimental profiles and their uncertainties, respectively, lie very close to the kink/peeling mode stability boundary.

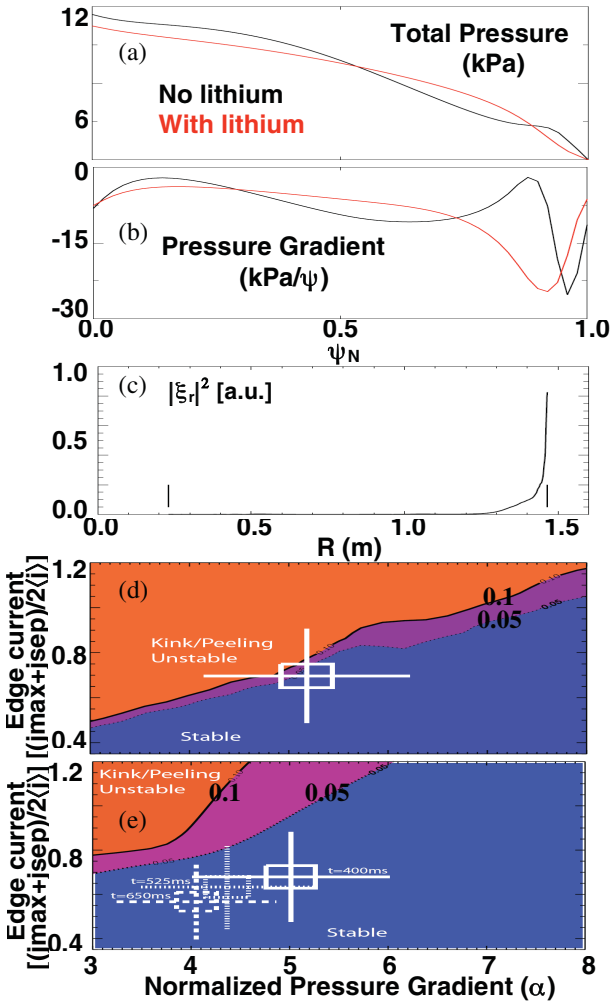

FIG. 3 (color). (a) Kinetic pressure and (b) pressure gradient in normalized flux space for the pre- and post-lithium equilibria; (c) radial displacement of $n = 3$ mode from PEST, with the calculation outer boundary at $\psi_N = 0.99$ given by the black vertical lines; stability boundary (blue to orange color transition) from ELITE code with fixed boundary kinetic EFITs for (d) pre-lithium discharge and (e) post-lithium discharge.

This boundary is the transition from the blue to the orange region, which corresponds with $\gamma/\omega_* > 5\%$. While this is an alternate stability threshold criterion than was used for assessment with PEST as discussed above, this stability criterion takes into account that rapid diamagnetic drift can stabilize peeling or ballooning modes [24]. The most unstable mode from ELITE had $n = 4$, i.e., relatively low-n in agreement with the PEST calculation.

As in the PEST calculations above, the post-lithium discharges were computed to be stable with ELITE [e.g., Fig. 3(e) showing three time slices from no. 129038], owing to two reasons: (1) The peak pressure gradient and calculated edge bootstrap current peak were shifted inboard to a region of reduced magnetic shear, which is stabilizing for the ballooning drive of these coupled peeling-ballooning modes, and (2) the peak pressure gradient was modestly reduced by up to 10%–20%, which is

also stabilizing. These coupled changes to the edge current and pressure profiles resulted in movement of the stability boundary relative to the profile parametrization in Fig. 3, possibly giving access to second stability.

The prediction that low-n modes are the most unstable for the pre-lithium discharges is in good agreement with analysis of the NSTX fast magnetics data for ELM precursors, as also seen in other devices [2,29]. Fitted precursor mode numbers from fast magnetics data were all low-n, with a general increase as the density and collisionality ramped during the discharge [e.g., Fig. 1(c)]. The mode frequency varied between 40 and 60 kHz with no clear time dependence. In contrast, precursor oscillations were not observed in the post-lithium ELM-free discharges.

In summary, lithium-wall coatings suppressed ELMs in otherwise ELMy NSTX discharges, owing ostensibly to reduction in both recycling and core fueling. The plasma profiles changed substantially as a result, with the n_e profile shifting radially inward by several centimeters. We note that, while the assumed core fueling reduction implies a reduction in the core particle outflux in steady state, the density gradient is also reduced, making it difficult to assess if the diffusion coefficient was modified. On the other hand, the cross-field electron thermal diffusivity from TRANSP [30] was shown to be reduced in the outer half of the plasma minor radius in other lithium-enhanced ELM-free discharges [16]. Ultimately, the change in the density profile shifted the steep pressure gradient to lower magnetic shear, which helped to stabilize the peeling and ballooning instabilities. Specifically the pre-lithium (post-lithium) profiles were unstable (stable) to $n = 2$–4 peeling or ballooning modes, based on calculations from two different codes. That these were low-n instabilities is supported by observations of precursor oscillations in the fast magnetics data, which were present in the pre-lithium discharges and absent in post-lithium discharges. We note there are uncertainties in our procedure, particularly the lack of an edge current measurement.

The discharges enabled by the lithium conditioning become ELM-free with a substantial improvement in energy confinement time relative to scalings. Consequently, the discharges achieved normalized beta β_N of 5.5, where $\beta_N = aB\beta/I_p$, a = minor radius, B_t = vacuum toroidal magnetic field on axis, β = ratio of plasma stored energy (W_{MHD}) to toroidal magnetic field stored energy ($B_t^2/2\mu_0$), μ_0 = permeability of free space, and I_p = plasma current. The global instability that terminated the high performance phase in Fig. 1 had characteristic signatures of a resistive wall mode, indicating that the discharge was operating between the ''no-wall'' and ''ideal-wall'' β limits in the NSTX [31]. In other words, the lithium-enhanced discharges reached global stability limits before reaching edge/ELM stability limits, thereby avoiding large pulsed power loads to the target. Looking ahead, quantitative understanding of the effect of the lithium-wall coatings on the density profile remains an area of active research for projection of the effects of lithium in other devices.

This research was supported by the U.S. Department of Energy under Contracts No. DE-AC05-00OR22725, No. DE-AC02-09CH11466, No. DE-FC02-04ER54698, and No. DE-FG02-99ER54524. We thank L. E. Zakharov for valuable discussions and acknowledge his prediction of ELM suppression with lithium coatings (due to a different mechanism) in advance of lithium experiments in the NSTX. The contribution of the NSTX technical and neutral beam operations staff is also gratefully acknowledged.

[1] F. Wagner *et al.*, Phys. Rev. Lett. **49**, 1408 (1982).
[2] H. Zohm *et al.*, Plasma Phys. Controlled Fusion **38**, 105 (1996).
[3] J. W. Connor *et al.*, Plasma Phys. Controlled Fusion **40**, 191 (1998).
[4] P. B. Snyder *et al.*, Phys. Plasmas **9**, 2037 (2002).
[5] H. R. Wilson *et al.*, Phys. Plasmas **9**, 1277 (2002).
[6] C. M. Greenfield *et al.*, Phys. Rev. Lett. **86** 4544 (2001).
[7] T. E. Evans *et al.*, Phys. Rev. Lett. **92**, 235003 (2004).
[8] R. Maingi *et al.*, Nucl. Fusion **45**, 1066 (2005).
[9] M. Ono *et al.*, Nucl. Fusion **40**, 557 (2000).
[10] A. R. Field *et al.*, Plasma Phys. Controlled Fusion **46**, 981 (2004).
[11] R. Maingi *et al.*, Plasma Phys. Controlled Fusion **46**, A305 (2004).
[12] V. A. Soukhanovskii *et al.*, J. Nucl. Mater. **313–316**, 573 (2003).
[13] R. J. Akers *et al.*, Phys. Rev. Lett. **88**, 035002 (2002).
[14] M. A. Mahdavi *et al.*, J. Nucl. Mater. **220–222**, 13 (1995).
[15] H. W. Kugel *et al.*, J. Nucl. Mater. **363–365** 791 (2007).
[16] H. W. Kugel *et al.*, Phys. Plasmas **15**, 056118 (2008).
[17] D. K. Mansfield *et al.*, J. Nucl. Mater. (to be published).
[18] H. W. Kugel *et al.*, J. Nucl. Mater. (to be published).
[19] R. Kaita *et al.*, in Proceedings of the 22nd Fusion Energy Conference, Geneva, 2008, paper EX/P4 (unpublished).
[20] S. F. Paul *et al.*, J. Nucl. Mater. (to be published).
[21] J. M. Canik *et al.*, in Proceedings of the 22nd Fusion Energy Conference, Geneva, 2008, paper PD/P1 (unpublished).
[22] S. M. Kaye *et al.*, Nucl. Fusion **37**, 1303 (1997).
[23] T. H. Osborne *et al.*, J. Phys. Conf. Ser. **123**, 012014 (2008).
[24] P. B. Snyder *et al.*, Nucl. Fusion **47**, 961 (2007).
[25] L. L. Lao *et al.*, Nucl. Fusion **25**, 1611 (1985).
[26] O. Sauter *et al.*, Phys. Plasmas **6**, 2834 (1999).
[27] R. Grimm *et al.*, Methods Comput. Phys. **16**, 253 (1976).
[28] P. B. Snyder *et al.*, Plasma Phys. Controlled Fusion **46**, A131 (2004).
[29] S. M. Kaye *et al.*, Nucl. Fusion **12**, 2621 (1990).
[30] R. J. Hawyrluk *et al.*, in *Physics of Plasmas Close to Thermonuclear Conditions* (Commission of the European Communities, Brussels, 1979), Vol. 1, p. 19.
[31] S. A. Sabbagh *et al.*, Nucl. Fusion **46**, 635 (2006).